

# Multifunctional $\text{Li}(\text{Ni}_{0.5}\text{Co}_{0.2}\text{Mn}_{0.3})\text{O}_2$ -Si batteries with self-actuation and self-sensing

Jun Ma<sup>1</sup> , Cody Gonzalez<sup>1</sup>, Qingquan Huang<sup>2</sup>, Joseph Farese<sup>1</sup>, Christopher Rahn<sup>1</sup> , Mary Frecker<sup>1</sup> and Donghai Wang<sup>1</sup>

Journal of Intelligent Material Systems and Structures

2020, Vol. 31(6) 860–868

© The Author(s) 2020

Article reuse guidelines:

sagepub.com/journals-permissions

DOI: 10.1177/1045389X19898768

journals.sagepub.com/home/jim



## Abstract

Among anode materials for Li-ion batteries, Si is known for high theoretical capacity, low cost, large volume change, relatively fast capacity fade and significant stress-potential coupling. This article shows that a  $\text{Li}(\text{Ni}_{0.5}\text{Co}_{0.2}\text{Mn}_{0.3})\text{O}_2$ -Si battery can store energy, actuate with Si volume change and sense with stress-potential coupling. Experiments are conducted in an electrolyte-filled chamber with a glass window with  $\text{Li}(\text{Ni}_{0.5}\text{Co}_{0.2}\text{Mn}_{0.3})\text{O}_2$  cathodes and Si composite anodes. The Si anodes are single-side coated on Cu current collector with Si nanoparticles, polyacrylic acid binder and conductive carbon black in a porous composite structure. During charging, the battery stores energy, Li inserts in the cantilevered Si anodes and the cantilevers bend laterally. Discharging the battery releases the stored energy and straightens the Si cantilevers. Imposing deformation on the Si cantilevers at a fixed state of charge causes bending stress in the composite coating and a change in the open circuit potential. Testing at 1 Hz confirms that the Si composite responds to dynamic stress variations and with almost no phase lag, indicating the bandwidth of the stress-potential coupling in Si composite anodes is at least 1 Hz.

## Keywords

Multifunctional, Li-ion battery, Si, actuation, sensing

## 1. Introduction

Lithium ion batteries are widely used for high power and energy density applications such as portable devices, electric vehicles and drones (Kempton, 2004; Scrosati et al., 2011). Among anode materials for next-generation lithium ion batteries, Si is known for its high theoretical capacity (4200 mA h/g (Obrovac and Christensen, 2004) compared to graphite's theoretical capacity of 372 mA h/g (Tarascon and Armand, 2001)) and relatively low price. Si exhibits over 300% volume change during cycling (Beaulieu et al., 2001), potentially providing large displacement for actuation. As shown in Table 1, the linear strain of Si when fully lithiated is only smaller than dielectric elastomer and larger than ferroelectric polymer, shape memory alloy and piezoelectric ceramic. The Young's modulus of Si is comparable to piezoelectric ceramic and shape memory alloy actuator materials and much higher than electrostrictive polymers. Lithiated Si can provide high actuation forces and large strains, potentially providing high actuation energy relative to existing actuator materials. Due to relatively slow Li-ion transport in Li-ion batteries, however, the actuation speed is

relatively low. Although the high volume change can cause significant voltage hysteresis (low cycle efficiency) (Lu et al., 2016), fracture active material particles and accelerate capacity fade (Christensen and Newman, 2006a, 2006b; McDowell et al., 2013), researchers found that using sufficiently small Si particles (<150 nm) in a compliant, conductive matrix can improve battery performance, reduce cracking and achieve hundreds of cycles (Chen et al., 2013; Mazouzi et al., 2015; Song et al., 2014a, 2014b; Yi et al., 2013).

Si anodes also demonstrate significant stress-potential coupling (Sethuraman et al., 2010). Under compression, the open circuit potential (OCP) of

<sup>1</sup>Department of Mechanical Engineering, The Pennsylvania State University, University Park, PA, USA

<sup>2</sup>Department of Materials Science and Engineering, The Pennsylvania State University, University Park, PA, USA

## Corresponding author:

Christopher Rahn, Department of Mechanical Engineering, The Pennsylvania State University, University Park, PA 16802, USA.  
Email: cdrahn@psu.edu

**Table 1.** Performance metrics for representative actuator materials.

Actuator	Maximum actuation strain	Young's modulus (GPa)	Maximum stress (GPa)	Maximum frequency (Hz)
Si <sup>a</sup>	59%	20 – 90	1	$<3 \times 10^{-3}$
Dielectric elastomer <sup>b</sup>	380%	0.02	0.072	0.2 – 1
Ferroelectric polymer <sup>c</sup>	10%	0.45	0.045	1
Shape memory alloy <sup>d</sup>	7%	30 – 90	0.2	$2 \times 10^{-2} - 7$
Piezoelectric ceramic <sup>d</sup>	0.2%	50 – 300	0.11	$5 \times 10^5 - 3 \times 10^7$

<sup>a</sup>Berla et al. (2015), McDowell et al. (2013) and Shenoy et al. (2010).<sup>b</sup>Brochu and Pei (2010).<sup>c</sup>Xu et al. (2001).<sup>d</sup>Huber et al. (1997).**Table 2.** Performance metrics for self-powered stress sensors.

Sensor	Sensitivity	Size (mm)	Self-power source	Bandwidth (Hz)
Si <sup>a</sup>	110 mV/GPa 8.7 mV/N 0.2 – 4 F/GPa	15×15×0.5	Energy storage (350 mW h/g) with low leakage	Unknown theoretically infinite
Piezoelectric <sup>b</sup>	10 V/N	20×10×0.2	Energy harvesting from continuous cyclic stress	500 – 1300
Capacitive <sup>c</sup>	0.01 – 0.5 $\mu$ F/GPa	5×5×0.03	Energy storage (1 – 15 mW h/g) with high leakage	350 – 1000

<sup>a</sup>Sethuraman et al. (2010).<sup>b</sup>Hajati and Kim (2011) and Ng and Liao (2005).<sup>c</sup>Albrecht et al. (2005) and Dobrzynska and Gijjs (2012).

lithiated Si is lower than the stress-free potential. Under tension, the OCP is higher than the stress-free potential. Previous experimental research with lithiated Si thin films measured an approximately linear stress-potential relationship and a stress-potential coupling factor of 110 mV/GPa (Sethuraman et al., 2010). The stress-potential coupling factor was found to be independent of the lithiation level. Compared with the other self-powered stress sensors listed in Table 2, the sensitivity of Si anodes is smaller than that of piezoelectric sensors but much larger than capacitive sensors, due to Si's high theoretical capacity. Li-ion batteries have very low self-discharge, so the expected sensor life can be several months. The sensor size can be as small as a coin cell. The bandwidth of the stress-potential or Larché–Cahn potential (Larché and Cahn, 1973, 1978, 1982) is theoretically infinite, so the sensing bandwidth could be quite high.

The unique properties of Si have inspired various device designs. The volume expansion of Si causes LFP-Si pouch cells to change thickness during cycling, which can be used for actuation purposes (Lang et al., 2016). Composite Si anode as unimorph cantilevers are designed and tested to determine coating layer modulus (Xie et al., 2016). Based on stress-potential coupling, lithiated Si-Si symmetric batteries are fabricated for energy harvesting (Kim et al., 2016). However, none of

previous research has developed multifunctional Si-based batteries that store energy, actuate during charging and sense stress state at the same time.

Figure 1 shows a schematic of the experimental testbed used to assess the energy storage, actuation and sensing capabilities of the Si anode. Si as the battery anode active material is single-side coated on a Cu current collector. One end of the anode is clamped and the other end is free, forming a unimorph cantilever configuration. The Si anode is paired with a  $\text{Li}(\text{Ni}_{0.5}\text{Co}_{0.2}\text{Mn}_{0.3})\text{O}_2$  (NCM) cathode. Soaked in electrolyte, the pair is able to store energy during charging and provide power to an external load during discharging. During charging, Li ions migrate from the cathode, through the electrolyte and insert in the Si anodes, causing the coating layer to expand. With the Cu current collector constraining axial motion, the anodes deform away from the cathode. During discharging, Li ions migrate back to cathode, reversing the bending motion. Thus, the electrode deformation is dependent on battery state of charge (SOC). When an external load changes the anode shape, stress-potential coupling results in a battery voltage change. The battery voltage at equilibrium is the potential difference between cathode and anode. When the Si coating is compressed, its potential decreases, resulting in a battery voltage increase. In contrast, when the Si coating is stretched,

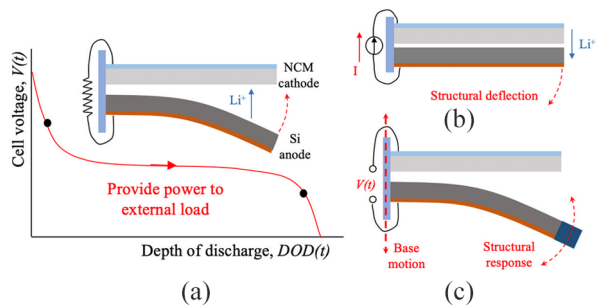


**Figure 1.** NCM-Si experimental testbed: (a) Energy storage and power supply to external load, (b) actuation with structural deflection during charging and (c) sensing via voltage output in response to base motion.

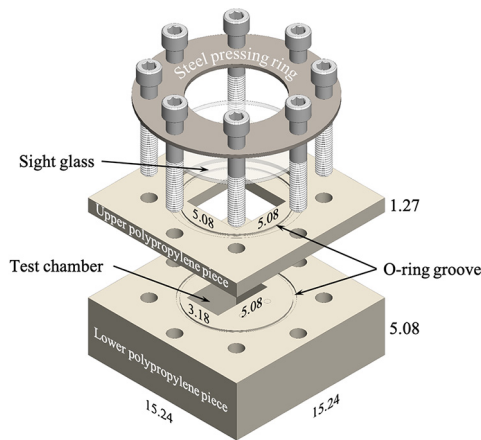


**Figure 2.** Experimental chamber design (length unit in centimetres).

its potential increases, leading to a battery voltage drop. By monitoring battery voltage, one can sense the stress state of Si anode.

In this article, we present the design, fabrication and testing of a transparent NCM-Si battery that allows measurement of voltage, current, cantilevered anode bending displacement under charge/discharge and applied loads. A unimorph composite beam model is presented to predict anode coating layer strain as a function of battery SOC.

## 2. Multifunctional battery design and fabrication

Figure 2 shows the NCM-Si chamber design consisting of two polypropylene (PP) pieces, a borosilicate glass disc, two O-rings and a steel pressing ring held in place by eight Allen screws. The O-rings are

**Table 3.** Anode parameters for experimental tests.

	Actuation	Sensing
Number of anodes (pcs)	4	1
Anode width (mm)	4	4
Anode length (mm)	30	18
Anode proof mass (mg)	0/56.320	168.960
Cu foil thickness ( $\mu\text{m}$ )	34	12
Cu foil Young's modulus (GPa)	120	120
Coating thickness ( $\mu\text{m}$ )	6	24
Coating Young's modulus (GPa)	1	5
Anode loading ( $\text{mg}/\text{cm}^2$ )	0.566	1.358

FEP-encapsulated with silicon cores that offer chemical compatibility with the battery electrolyte.

The testbed chamber houses the battery core with one NCM cathode and multiple Si anode cantilevers. The NCM cathode coating consists of NCM particles (94.2 wt%, average particle diameter  $10\text{ }\mu\text{m}$ ), polyvinylidene fluoride (PVDF) binder (2.9 wt%) and carbon black (CB) conductive additive (2.9 wt%). The single-sided coating is nominally  $44\text{ }\mu\text{m}$  thick and the Al current collector is  $15\text{ }\mu\text{m}$  thick. The NCM active material loading is  $12.1\text{ mg}/\text{cm}^2$ . The cathode is inserted into a separator pouch that electrically insulates the anodes while allowing lithium ion transport. The pouch is made of two pieces of Celgard 2320 separator. The separators are heat sealed on three edges. The last edge is left open for cathode insertion and electrical connection. An Al wire serves as the positive terminal, connecting to the NCM cathode through resistance welding.

The anode coating consists of Si nanoparticles (average particle diameter of  $50\text{ nm}$ ), polyacrylic acid (PAA) binder and CB conductive additive. The three components are dissolved in deionized water to form uniform slurry. The slurry is then coated on a Cu current collector. After drying, the coating layer is porous (approximate porosity of 60%). The coated sheet is then cut into rectangular strips, and their dimensions are shown in Table 3. One end of each anode is connected to a 24-gauge Cu wire through resistance welding. The welding provides a clamped boundary condition. The Cu wires are polytetrafluoroethylene (PTFE) insulated, allowing measurement of individual anode potentials.

Prototypes are shown in Figure 3. Two tests are performed, one for actuation and one for sensing. In the actuation test (Figure 3(a)), the NCM cathode is attached to a PP substrate. Four Si anode strips are paired with the cathode, with their coated sides (3:1:1, Si:PAA:CB) facing towards NCM coating. In the sensing test (Figure 3(b)), the Si anode is perpendicular to the NCM cathode. This orientation helps eliminate any

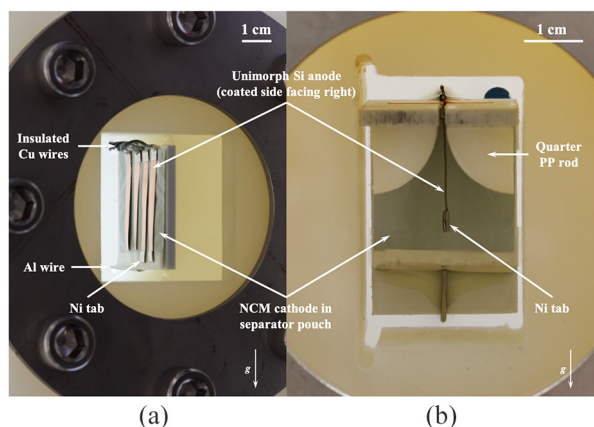


**Figure 3.** Battery prototype in the (a) actuation test and (b) sensing test.

possible capacitance effect that might affect the measured voltage. The Si anode is located between two quarter cut PP rods (diameter 12.7 mm). With this setup, the anode is able to deform in both compression and tension during shaking.

The entire device is dried in a vacuum oven at 80°C for 24 h prior to moving into a glovebox for electrolyte filling.

The electrolyte is 1M  $\text{LiPF}_6$  in ethylene carbonate (EC) and ethyl methyl carbonate (EMC) solution (1:1 by volume). The electrolyte is added through a filling port located on the backside of the test chamber. After filling, the filling port is sealed with a chemical-resistant plug.

### 3. Experimental

#### 3.1. Actuation test

In the actuation test, the prototype battery is cycled on a Landt A2000 coin cell tester at room temperature. During this electrochemical actuation test, the four anodes are cycled in parallel using one channel of the tester. The charge and discharge cycles are performed with constant current at approximately C/20 rate (20 h for full charge or 0.26 mA). To ensure the anode deflections are within the material elastic region, the cell is not fully charged to the cutoff voltage (4.20 V). The device rests for 5 min followed by constant current C/20 discharge. During the test, the anode cantilevers are oriented vertically with the free end pointing downwards as shown in Figure 4(a). A digital camera with a macro lens captures the deformation process with one picture taken every 30 s.

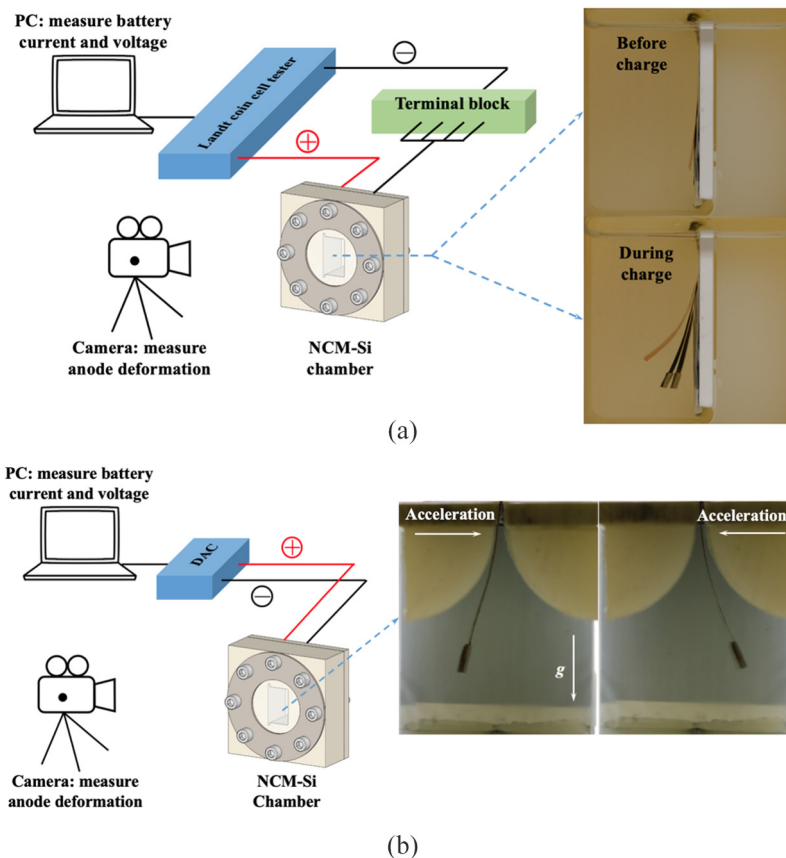


**Figure 4.** Test setups for NCM-Si testbed: (a) In actuation test, the four anodes are cycled in parallel oriented vertically and (b) in sensing test, a DAC measures battery voltage during horizontal shaking.

### 3.2. Sensing test

In the sensing test, a heavy (relative to the cantilever) proof mass on the tip of the Si anode makes the cantilever to deform when the chamber is accelerating as shown in Figure 4(b). To ensure uniform lithiation across the anode width, the battery is charged at C/80 rate (80 h for full charge or 0.036 mA). After reaching the desired lithiation level, the battery is disconnected from the coin cell tester, rested for 12 h to allow Li redistribution and reconnected to a DAC (Measurement Computing, USB-2408). The DAC monitors the battery voltage response at a 10 Hz sampling rate. Sliding the chamber back and forth along a smooth horizontal surface causes dynamic bending of the Si cantilever. In this test, the battery is rested for 1 min, followed by horizontal vibration at 1 Hz for 1 min. During vibration, the chamber moves laterally  $\pm 10$  cm. At the rightmost position, the proof mass has maximum leftward acceleration and the coating layer is compressed. At the leftmost position, the proof mass has maximum rightward acceleration and the coating layer is stretched. The vibration test is repeated for five times to demonstrate repeatability.

### 4. Unimorph cantilever model

To calculate Si coating layer stress and strain based on measured tip deflection, a unimorph cantilever model is developed that neglects gravitational loading and assumes that the unimorph has constant curvature  $\kappa$  along its length. From the geometry in Figure 5

$$\kappa d + \cos(\kappa L) - 1 = 0 \quad (1)$$

where  $d$  is the anode tip displacement and  $L$  is the anode length. Equation (1) is solved numerically for  $\kappa$  as a function of  $d$ . We assume the following: (1) coating layer expansions in the  $y$  and  $z$  directions are neglected, (2) the coating layer is continuous and uniform material with material properties independent of lithium concentration and (3) the coating layer is perfectly bonded to the current collector.

From the free-body diagram in Figure 5, beam equilibrium condition requires

$$N_{ct} = N_{Cu} = N \quad (2)$$

where  $N_{ct}$  and  $N_{Cu}$  are the axial forces of the anode coating and copper current collector, respectively. The moment balance

$$M_{ct} + M_{Cu} = \frac{N}{2}(h_{ct} + h_{Cu}) \quad (3)$$

where  $M_{ct}$  and  $M_{Cu}$  are the bending moments and  $h_{ct}$  and  $h_{Cu}$  are thicknesses of the coating layer and copper layer, respectively. Assuming a linear moment curvature relationship

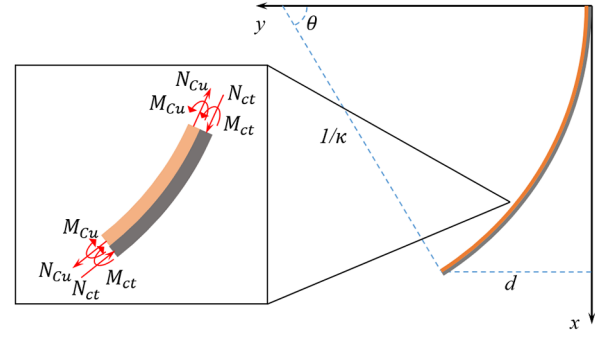


**Figure 5.** Anode tip displacement and curvature geometry and unimorph cantilever free-body diagram (inset).

$$M_{ct} + M_{Cu} = \kappa(E_{ct}I_{ct} + E_{Cu}I_{Cu}) \quad (4)$$

where  $E_{ct}$  and  $E_{Cu}$  are Young's moduli of the coating and current collector, respectively. The coating and current collector area moments of inertia

$$I_{ct} = \frac{1}{12}Wh_{ct}^3 + Wh_{ct}\left(\frac{h_{ct}}{2} + h_{Cu} - h_n\right)^2 \quad (5)$$

$$I_{Cu} = \frac{1}{12}Wh_{Cu}^3 + Wh_{Cu}\left(h_n - \frac{h_{Cu}}{2}\right)^2 \quad (6)$$

where the position of neutral axis

$$h_n = \frac{E_{Cu}\frac{h_{Cu}^2}{2} + E_{ct}h_{ct}(h_{Cu} + \frac{h_{ct}}{2})}{E_{Cu}h_{Cu} + E_{ct}h_{Cu}} \quad (7)$$

The non-slip interface condition requires that

$$S - \frac{N_{ct}}{E_{ct}A_{ct}} - \kappa\frac{h_{ct}}{2} = \frac{N_{Cu}}{E_{Cu}A_{Cu}} + \kappa\frac{h_{Cu}}{2} \quad (8)$$

where  $S$  is the actuation strain of the Si coating layer due to Li insertion. Combining equations (2), (3), (4) and (8), we obtain the actuation strain

$$S = \kappa\frac{2(E_{ct}I_{ct} + E_{Cu}I_{Cu})(E_{ct}A_{ct} + E_{Cu}A_{Cu})}{(h_{ct} + h_{Cu})E_{ct}A_{ct}E_{Cu}A_{Cu}} + \kappa\frac{h_{ct} + h_{Cu}}{2} \quad (9)$$

## 5. Results and discussion

### 5.1. Energy storage

Figure 6 shows the experimental electrochemical performance in the actuation test. Fourteen cycles are conducted with constant current charge to 3.78–4.00 V (charge cutoff voltage gradually increases from 3.78 V to 4.00 V in the first 6 cycles and then fixed at 4.00 V) at a C/20 rate and constant current discharge to 2.00 V. The battery voltage curves in Figure 6(a) show energy storage during charging and energy supply during subsequent discharging, sourcing 2.07 mWh during the first



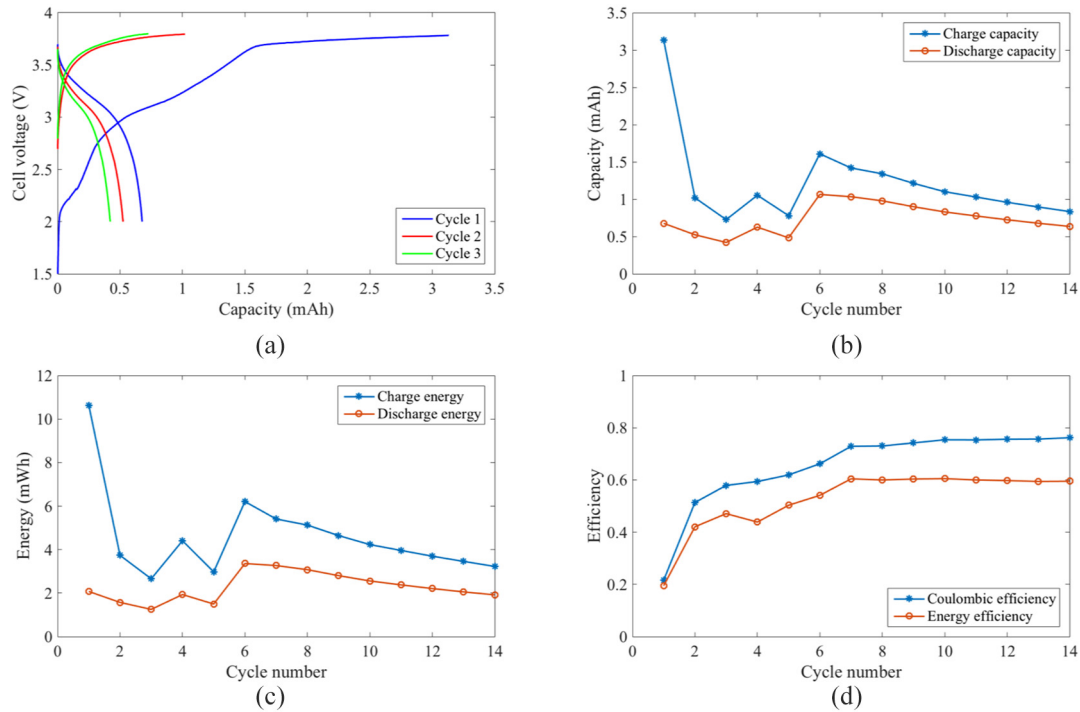


**Figure 6.** Experimental electrochemical performance during actuation test: (a) Charge and discharge curves at a C/20 rate, (b) charge and discharge capacity versus cycle number, (c) charge and discharge energy versus cycle number and (d) coulombic and energy efficiency versus cycle number.

cycle and a peak of 3.36 mWh in cycle 6. The capacity shown in Figure 6(b) drops quickly during the first cycle (charge capacity is 3.13 mA h and discharge capacity is 0.68 mA h). The charge/discharge energy in Figure 6(c) also fades significantly during the first cycle. The low first cycle efficiency is attributed to two effects: (1) The first lithiation process of Si is associated with phase transition from crystalline Si to amorphous Si. This transition involves plastic deformation that is not reversible. (2) Solid-electrolyte interphase (SEI) formation irreversibly consumes Li ions (McDowell et al., 2013).

As shown in Figure 6(d), both coulombic and energy efficiencies increase gradually from cycle 1 to cycle 6 and then stabilize, probably due to completion of SEI formation. The coulombic efficiency is around 75%, and the energy efficiency is around 60%. The battery's coulombic efficiency is significantly lower than that of a Si-Li coin cell, which has been measured greater than 90% after 100 cycles (Song et al., 2014b). The large and non-uniform gap between the anode and cathode is partially responsible for this effect.

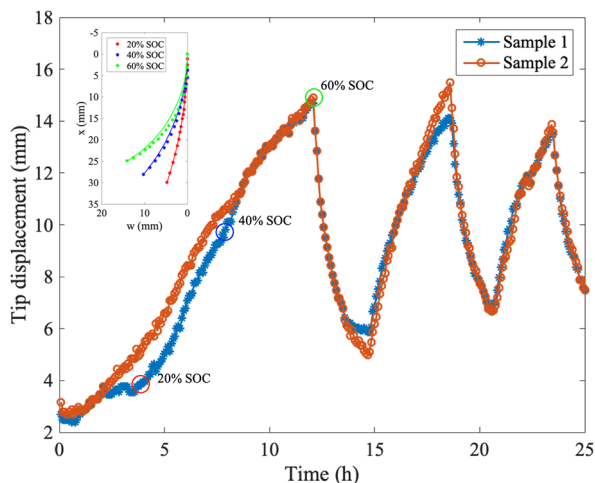
## 5.2. Actuation

Figure 7 shows the tip displacement of two anodes in the first 3 cycles. The displacement is 2.92 mm at the beginning of the test, due to the binder swelling after electrolyte filling. The tip displacement increases slowly

with battery SOC in first 5 h, possibly due to Si particles expanding into pores. This effect is only observed in the first cycle, indicating it is an irreversible plastic deformation process. The charge stops at 60% of the theoretical maximum SOC to prevent possible delamination of the Si coating from the current collector. The average maximum tip displacement is 14.80 mm. Constant current discharge brings the tip displacement back to 5.43 mm, completing the first cycle. The subsequent two cycles produce 14.80 and 13.72 mm maximum tip displacement, while the minimum displacement increases to 6.65 and 7.29 mm, respectively. This rapid degradation of stroke from 9.37 to 6.43 mm in 3 cycles is possibly due to mechanical failure to the Si anode due to the large strain. The displacements of the two samples match well, indicating the observed actuation is repeatable.

The inset in Figure 7 shows that the anodes maintain approximately circular shape (constant curvature along beam length) during cycling. The solid lines are constant curvature arcs and the stars are the anode shape sample points extracted from digital images. The normalized root mean square (RMS) error

$$err = \frac{\sqrt{\sum (w_{sample} - w_{arc})^2}}{\sqrt{\sum w_{sample}^2}} \quad (10)$$



**Figure 7.** Experimental tip displacement of two anodes in the first 3 cycles. Inset shows the experimentally measured (star) and constant curvature model (solid) anode shapes at 20% (red), 40% (blue) and 60% (green) battery SOC.

is smallest at low SOC (2.6%) and remains below 10% for all cases, showing that the constant curvature assumption is reasonable and the coating strain is approximately uniform.

Figure 8 shows the actuation strain of the coating later in the second and third cycle. The curvature is calculated from the measured tip displacement using equation (1) and the strain is calculated from equation (9). The SOC is calculated with the experimental capacity measurement divided by battery theoretical capacity (5.2 mA h). The SOC strain relationship is hysteretic and non-stationary, symptomatic of SEI layer formation, plastic deformation and a degrading coating. The average slope of the two samples during charge is approximately half of the theoretically predicted linear strain of Si particles based on reported 300% volume change. The other half of actuation strain is absorbed by the porous and soft structure of the composite electrode.

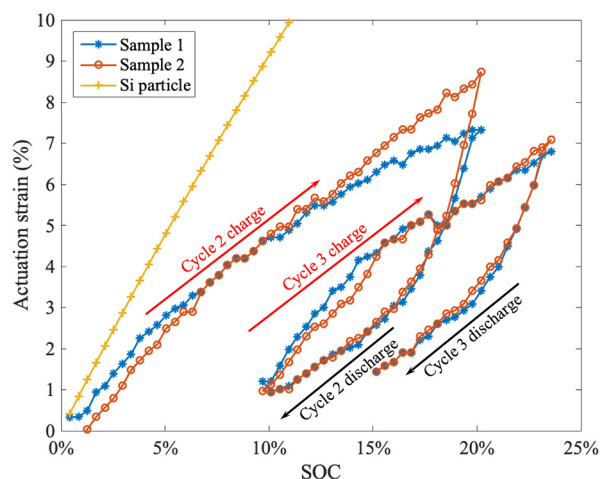


**Figure 8.** Comparison of actuation strain between Si nanoparticle and anode coating layer.

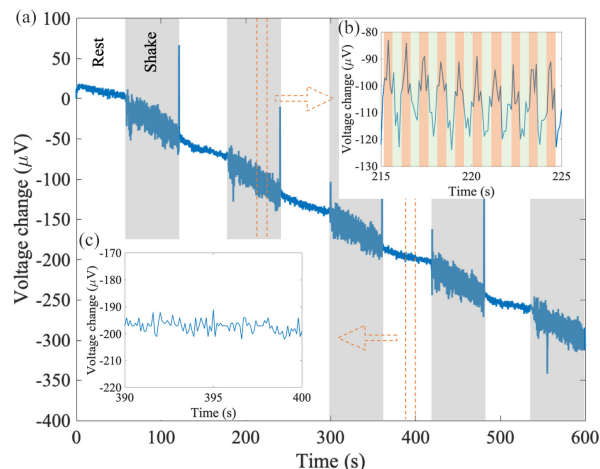


**Figure 9.** Change in battery voltage from 3.9356 V (80% SOC) with 1 Hz horizontal vibration. The voltage (a) shows slow decay due to Li redistribution and periodic response during vibration (grey highlights and inset (b)) and noise during static periods (no highlight and inset (c)). The orange and green highlights in (b) correspond to times when the anode coating is in compression and tension, respectively.

### 5.3. Sensing

For the sensing test, the Si anode is first lithiated to a desired SOC. During lithiation, the anode remains approximately straight due to the heavy proof mass and vertical chamber orientation. After lithiation, the battery is rested for 12 h, disconnected from the coin cell tester and connected to a DAC to measure battery voltage.

Figure 9 shows the vibration test conducted at 3.9356 V OCP (80% battery SOC or 2800 mA h/g). The grey bands in Figure 9(a) correspond to times when the chamber, with the anode cantilever hanging vertically,

is moved horizontally with an amplitude of 10 cm and a frequency of 1 Hz. The OCP shows increased activity during these times as opposed to when the chamber is not vibrating. The inset in Figure 9(b) shows the zoomed-in voltage response during vibration. The periodic voltage response can be seen, and it is in phase with the stress caused by base acceleration. The stress-potential coupling is negative for compressive stress and positive for tensile stress. Near-zero phase lag means the bandwidth for stress-potential coupling in Si anodes is greater than 1 Hz.

## 6. Conclusion

This article shows that composite Si anodes can store energy, actuate through volume change associated with lithium insertion and sense stress through stress-potential coupling. Experimental results show a Cu current collector single-side coated with Si nanoparticles can store 10.6 mW h (charge)/2.1 mW h (discharge) energy and bend laterally with over 40% beam length displacement. Using a unimorph cantilever model, the Si coating layer actuation strain is estimated to be 27.8% at 100% SOC, less than half of the theoretical strain of pure Si. Dynamic stress tests at 1 Hz show in-phase stress-potential coupling, suggesting a bandwidth of at least 1 Hz.

Both the actuation and sensing tests have large gaps between NCM cathodes and Si anodes. The gap is a possible explanation for reduced battery performance. The large gap introduces a much longer electrolyte phase ionic transportation path than that in conventional Li-ion batteries. As a consequence, the battery voltage reaches the cutoff condition much earlier due to higher internal voltage loss during discharging. In future tests, battery cathode and anode should deform together to keep the gap minimum and constant. Besides, the presented battery design lacks pressure on the electrode surface, which is critical for coating layer mechanical integrity. The absence of pressure may cause debonding between the coating layer and Cu current collector during large actuation and repeated mechanical stress, resulting in smaller voltage response during shaking test at 80% SOC.

Since the coating layer actuation strain estimation is based on experimental data, the result depends on battery fabrication quality, measurement accuracy and test repeatability. For example, Si coating layer thickness may not be uniform across anode length due to imperfect fabrication. Further tests are still needed to validate the results with different electrode design parameters. Besides, in the unimorph cantilever model, the coating layer homogeneous modulus is assumed to be constant. However, as Si particles change volume, the coating layer porosity and composite volume fraction are also changing. Therefore, a more detailed analysis of coating layer modulus as a function of battery SOC is recommended.

## Acknowledgements

The authors gratefully acknowledge the support of the National Science Foundation under Grant No. 1662055.

## Declaration of conflicting interests


The author(s) declared no potential conflicts of interest with respect to the research, authorship and/or publication of this article.

## Funding

The author(s) received no financial support for the research, authorship and/or publication of this article.

## ORCID iDs

Jun Ma  <https://orcid.org/0000-0002-2425-9784>

Christopher Rahn  <https://orcid.org/0000-0002-6670-5674>

## References

- Albrecht A, Park S, Altintas Y, et al. (2005) High frequency bandwidth cutting force measurement in milling using capacitance displacement sensors. *International Journal of Machine Tools and Manufacture* 45(9): 993–1008.
- Beaulieu LY, Eberman KW, Turner RL, et al. (2001) Colossal reversible volume changes in lithium alloys. *Electrochemical and Solid-State Letters* 4(9): A137–A140.
- Berla L, Lee S, Cui Y, et al. (2015) Mechanical behavior of electrochemically lithiated silicon. *Journal of Power Sources* 273: 41–51.
- Brochu P and Pei Q (2010) Advances in dielectric elastomers for actuators and artificial muscles. *Macromolecular Rapid Communications* 31(1): 10–36.
- Chen J, Liu J, Qi Y, et al. (2013) Unveiling the roles of binder in the mechanical integrity of electrodes for lithium-ion batteries. *Journal of the Electrochemical Society* 160(9): A1502–A1509.
- Christensen J and Newman J (2006a) A mathematical model of stress generation and fracture in lithium manganese oxide. *Journal of Solid State Electrochemistry* 15(6): A1019–A1030.
- Christensen J and Newman J (2006b) Stress generation and fracture in lithium insertion materials. *Journal of Solid State Electrochemistry* 10(5): 293–319.
- Dobrzynska J and Gijs M (2012) Polymer-based flexible capacitive sensor for three-axial force measurements. *Journal of Micromechanics and Microengineering* 23(1): 015009.
- Hajati A and Kim S (2011) Ultra-wide bandwidth piezoelectric energy harvesting. *Applied Physics Letters* 99(8): 083105.
- Huber J, Fleck N and Ashby M (1997) The selection of mechanical actuators based on performance indices. *Proceedings of the Royal Society of London A: Mathematical, Physical and Engineering Sciences* 453(1965): 2185–2205.
- Kempton W (2004) Electric vehicles: driving range. *Nature Energy* 1(9): 16131.
- Kim S, Choi SJ, Zhao K, et al. (2016) Electrochemically driven mechanical energy harvesting. *Nature Communications* 7: 10146.
- Lang J, Ding B, Zhu T, et al. (2016) Cycling of a lithium-ion battery with a silicon anode drives large mechanical actuation. *Advanced Materials* 28(46): 10236–10243.
- Larché FC and Cahn JW (1973) A linear theory of thermochemical equilibrium of solids under stress. *Acta Metallurgica* 21(8): 1051–1063.
- Larché FC and Cahn JW (1978) A nonlinear theory of thermochemical equilibrium of solids under stress. *Acta Metallurgica* 26(1): 53–60.
- Larché FC and Cahn JW (1982) The effect of self-stress on diffusion in solids. *Acta Metallurgica* 30(10): 1835–1845.



- Lu B, Song Y, Zhang Q, et al. (2016) Voltage hysteresis of lithium ion batteries caused by mechanical stress. *Physical Chemistry Chemical Physics* 18(6): 4721–4727.
- McDowell M, Lee S, Nix W, et al. (2013) 25th anniversary article: understanding the lithiation of silicon and other alloying anodes for lithium-ion batteries. *Advanced Materials* 25(36): 4966–4985.
- Mazouzi D, Karkar Z, Hernandez C, et al. (2015) Critical roles of binders and formulation at multiscales of silicon-based composite electrodes. *Journal of Power Sources* 280: 533–549.
- Ng T and Liao W (2005) Sensitivity analysis and energy harvesting for a self-powered piezoelectric sensor. *Journal of Intelligent Material Systems and Structures* 16(10): 785–797.
- Obrovac MN and Christensen L (2004) Structural changes in silicon anodes during lithium insertion/extraction. *Electrochemical and Solid-State Letters* 7(5): A93–A96.
- Scrosati B, Hassoun J and Sun YK (2011) Lithium-ion batteries. A look into the future. *Energy & Environmental Science* 414(6861): 3287–3295.
- Sethuraman VA, Srinivasan V, Bower A, et al. (2010) In situ measurements of stress-potential coupling in lithiated silicon. *Journal of the Electrochemical Society* 157(11): A1253–A1261.
- Shenoy V, Johari P and Qi Y (2010) Elastic softening of amorphous and crystalline Li-Si phases with increasing Li concentration: a first-principles study. *Journal of Power Sources* 195(19): 6825–6830.
- Song J, Chen S, Zhou M, et al. (2014a) Micro-sized silicon-carbon composites composed of carbon-coated sub-10 nm Si primary particles as high-performance anode materials for lithium-ion batteries. *Journal of Materials Chemistry A* 2(5): 1257–1262.
- Song J, Zhou M, Yi R, et al. (2014b) Interpenetrated gel polymer binder for high-performance silicon anodes in lithium-ion batteries. *Advanced Functional Materials* 24(37): 5904–5910.
- Tarascon JM and Armand M (2001) Issues and challenges facing rechargeable lithium batteries. *Nature* 414(6861): 359–367.
- Xie H, Qiu W, Song H, et al. (2016) In situ measurement of the deformation and elastic modulus evolution in Si composite electrodes during electrochemical lithiation and delithiation. *Journal of the Electrochemical Society* 163(13): A2685–A2690.
- Xu H, Cheng Z, Olson D, et al. (2001) Ferroelectric and electromechanical properties of poly (vinylidene-fluoride-trifluoroethylene-chlorotrifluoroethylene) terpolymer. *Applied Physics Letters* 78(16): 2360–2362.
- Yi R, Dai F, Gordin M, et al. (2013) Influence of silicon nanoscale building blocks size and carbon coating on the performance of micro-sized Si-C composite Li-ion anodes. *Advanced Energy Materials* 3(11): 1507–1515.